Zweitveröffentlichung/
Secondary Publication

Staats- und Universitätsbibliothek Bremen

https://media.suub.uni-bremen.de

Gleichauf, Daniel ; Dollinger, Christoph ; Balaresque, Nicholas ; Gardner, Anthony D. ; Sorg, Michael ; Fischer, Andreas

Thermographic flow visualization by means of non-negative matrix factorization

Journal Article as: peer-reviewed accepted version (Postprint)

DOI of this document*(secondary publication): https://doi.org/10.26092/elib/3325

Publication date of this document: 20/09/2024

* for better findability or for reliable citation

Recommended Citation (primary publication/Version of Record) incl. DOI:

Daniel Gleichauf, Christoph Dollinger, Nicholas Balaresque, Anthony D. Gardner, Michael Sorg, Andreas Fischer, Thermographic flow visualization by means of non-negative matrix factorization, International Journal of Heat and Fluid Flow, Volume 82, 2020, 108528, ISSN 0142-727X, https://doi.org/10.1016/j.ijheatfluidflow.2019.108528.

Please note that the version of this document may differ from the final published version (Version of Record/primary publication) in terms of copy-editing, pagination, publication date and DOI. Please cite the version that you actually used. Before citing, you are also advised to check the publisher's website for any subsequent corrections or retractions (see also https://retractionwatch.com/).

This document is made available under a Creative Commons licence.

The license information is available online: https://creativecommons.org/licenses/by-nc-nd/4.0/

Take down policy

If you believe that this document or any material on this site infringes copyright, please contact publizieren@suub.uni-bremen.de with full details and we will remove access to the material.

Thermographic flow visualization by means of non-negative matrix factorization

Daniel Gleichauf[*,a], Christoph Dollinger[b], Nicholas Balaresque[c], Anthony D. Gardner[d], Michael Sorg[a], Andreas Fischer[a]

[a] University of Bremen, Bremen Institute for Metrology, Automation and Quality Science, Linzer Str. 13, Bremen 28359, Germany
[b] former: University of Bremen, Bremen Institute for Metrology, Automation and Quality Science, Linzer Str. 13, Bremen 28359, Germany
[c] Deutsche WindGuard Engineering GmbH, Uberseering 7, Bremerhaven 27580, Germany
[d] German Aerospace Center (DLR), Bunsenstrasse 10, Göttingen 37073, Germany

ARTICLE INFO

Keywords:
Thermographic flow visualization
Boundary layer measurement
Computer vision
Temperature inhomogeneity
Non-negative matrix factorization
Contrast enhancement

ABSTRACT

In order to investigate the areas of different flow regimes in the boundary layer of an airfoil, thermography is a powerful flow visualization tool. However, the distinguishability between boundary layer flow regimes such as laminar or turbulent is limited due to systematic and random inhomogeneity in the measured temperature field, hindering a clear separation of the flow regimes. In order to increase the distinguishability of different flow regimes, a time series of thermographic images is evaluated by means of a non-negative matrix factorization. As a result, the non-negative matrix factorization creates images that contain the dominant features of the measured images, while reducing systematic temperature gradients within the flow regimes by up to a factor of five. This way an increase of the distinguishability between every pair of consecutive flow regimes can be achieved on the surface of a non-heated cylinder in cross-flow condition. As a further application example of the non-negative matrix factorization, the distinguishability between the flow and the laminar-turbulent transition zone on a heated helicopter airfoil is also increased by a factor of five. Hence, non-negative matrix factorization is capable of enhancing thermographic flow visualization for increasing the distinguishability of different flow phenomena.

1. Introduction

The boundary layer flow of an airfoil has a significant influence on the aerodynamic properties and thus on the efficiency of the energy conversion from the fluid to the airfoil or vice versa. For example, in the case of rotor blades on wind turbines, a 10 % increase in laminar flow leads to a reduction in drag of about 10 % (Bæk and Fuglsang, 2009). Furthermore, the existence of flow separation increases the drag and decreases the lift (Gad-el Hak and Bushnell, 1991) and plays an important role in the occurrence of stall at aircraft wings (Crawford et al., 2013) or helicopter rotor blades (Gardner et al., 2016). In order to understand the aerodynamic performance of an airfoil, a measurement of the boundary layer flow state is required. The main objective is to distinguish between laminar, turbulent and separated flow. Established flow visualization approaches use the interaction of the flow with supplements to achieve a distinction of different flow regimes through an optical observation. However, this includes a preparation of the surface with tufts (Swytink-Binnema and Johnson, 2016), stall flags (Corten and Veldkamp, 2001) or an oil film (Medina et al., 2011), which is time-consuming and influences the flow to be measured. Consequently, a faster and contactless flow visualization method is desired, which is able to cope with an unmodified airfoil surface.

A measurement approach that meets these demands is the thermographic flow visualization. Different flow states in the boundary layer flow have different friction correlated heat transfer coefficients between the fluid and the surface. Therefore, based on an initial temperature difference between the fluid and the surface, boundary layer flow regimes can be distinguished by means of the surface temperature (Quast, 1987; de Luca et al., 1990). The thermographic measurement of the surface temperature results in a non-contact, non-invasive measurement approach. So far, the thermographic flow visualization is an established method in wind tunnel measurements to localize the laminar-turbulent transition (Gartenberg et al., 1992) and to observe the existence of laminar separation bubbles (Montelpare and Ricci, 2004) or separated flow (Gartenberg and Roberts, 1991). Furthermore the contact-less localization of the laminar-turbulent transition and a comparison with it's nominal-position enables a quantification of flow disturbances caused by contamination or erosion of the leading

* Corresponding author.
E-mail address: d.gleichauf@bimaq.de (D. Gleichauf).

edge (Dollinger et al., 2019).

The main goal of thermographic flow visualization is the measurement of the geometrical dimensions of a boundary layer flow regime through locating its border to an adjoined flow regime. The uncertainty of this localization is directly dependent on the existence of a distinct surface temperature step between the two flow regimes (Dollinger et al., 2018b). Temporal and spatial temperature fluctuations (Dollinger et al., 2018b) superimposed with measurement noise add a random influence on the measured surface temperature of the flow regimes. Due to a non-constant heat flux in certain flow regimes (de Luca et al., 1990), a systematic temperature gradient in flow direction can occur, further reducing the homogeneity of the temperature pattern. The randomly and systematically influenced temperature inhomogeneity can decrease the visibility of the surface temperature step at the border between two adjoining flow regimes, which aggravates the distinguishability of neighbouring flow regimes.

In thermographic measurements with a high thermal contrast between the flow regimes, the impact of the temperature inhomogeneity on the flow visualization decreases. In-process experiments outside a laboratory environment typically hinder an additional heating of either the surface or the fluid to achieve the desired high thermal contrast. Hence an evaluation method for measurements with low thermal contrast is demanded that can lower the effects of the flow regimes' inhomogeneities in order to increase the distinguishability between them.

Another effect hindering a separation between the flow regimes with low uncertainty is the dynamic behaviour and the spatially unsharp transition between the flow regimes. Even at a high mean temperature difference, the borders of the laminar and the turbulent flow regimes are difficult to locate, because the transition does not take place immediately, but rather over a distance. According to Schlichting (1979) the laminar-turbulent transition is an area containing four distinct processes of the transformation from laminar to completely turbulent flow. At first, in the direction of flow, Tollmien-Schlichting-waves are formed and superimpose the laminar flow. Afterwards three dimensional structures form, creating vortices in a typical Λ-structure. Afterwards the vortices are decaying and transform into turbulent spots until the flow becomes completely turbulent. By investigating the laminar-turbulent transition concerning its position and length on a dynamically pitching DSA-9A helicopter airfoil, Richter et al. (2015) prove a dependency of position and size of the transition regarding the pitch angle. This spatial expansion of the transition results in an elongated temperature change between the laminar and turbulent flow regimes. Therefore no steep temperature gradient between the flow regimes and the transition area exists on the basis of which the borders of the flow regimes can be identified.

With the aim of improving the distinguishability between flow regimes on wind turbine rotor blades, Dollinger et al. (2018a) evaluated temporal temperature fluctuations of a thermographic image series. By means of a temporal standard deviation or by selecting specific Fourier coefficients of the temperature time series, an increase in the distinguishability can be achieved. Another application for images with low distinguishability between flow regimes was made by Gardner et al. (2016) while conducting dynamic measurements. Because of a heat flux from the surface layer into the measurement object and tangential to the surface, dynamically changing flow states resulted in a low contrast between the surface temperatures of different flow regimes. Therefore, Gardner et al. considered consecutive differential images in a time series of a high frequency pitching helicopter airfoil and evaluated the spatial standard deviations of the differential images. This method distinguishes between attached and detached flow for dynamically changing flow states with a frequency of up to 5 Hz. While Gardner et al. and Dollinger et al. have proven the evaluation of spatial or temporal temperature fluctuations due to the flow characteristics in order to improve the distinguishability of flow regimes, a simultaneous evaluation of temporal and spatial fluctuations was not yet investigated.

For this reason, an evaluation of the surface temperature information by an image processing method based on the feature extraction method non-negative matrix factorization (NMF) in order to increase the sensitivity of thermographic flow visualization is conducted. By evaluating the time and space domain through using time-resolved infrared images, the information about temporal and spatial temperature fluctuations in the flow regimes of a steady flow experiment are processed simultaneously by the NMF algorithm.

The hypothesis is that the NMF extracts feature images containing the information that increases the distinguishability through decreasing the effect of the systematic and random inhomogeneity. In order to evaluate this hypothesis, a well-studied type of measurement object, a circular cylinder in cross flow is chosen. By using a Reynolds number above the critical Reynolds number $Re_{crit} = 4.0 \times 10^5$ (Schlichting, 1979), the boundary layer flow around the cylinder develops a laminar flow, a laminar-separation bubble, a turbulent flow and a turbulent separated flow, allowing an evaluation of the distinguishability between all types of flow regimes on one surface. After evaluating the general use of the NMF approach, a more application orientated evaluation on a DSA-9A helicopter airfoil is conducted.

The basic principle of the thermographic flow measurement, the NMF method, as well as the definition of the homogeneity of flow regimes are explained in Section 2. The procedure is applied to two wind tunnel measurements using a cylinder model and a helicopter airfoil model. The experimental setup and results are described in Section 3 and Section 4, respectively. The article closes with a summary and an outlook in Section 5.

2. Measurement approach

2.1. Thermographic flow visualization

Depending on the friction correlated heat coefficients, different flow regimes develop different surface temperatures which are visualized by measuring the infrared radiation with a thermographic camera. In combination with the flow velocity v and the kinematic viscosity ν of the fluid, as well as the thermal conductivity λ_h of the fluid, according to Gartenberg et al. (1989), the heat transfer coefficient α_h at the position x depends on the friction coefficient $c_{f,x}$ and is calculated by

$$\alpha_{h,x} = \frac{1}{2} \cdot c_{f,x} \cdot \frac{\lambda_h \cdot v}{\nu}. \tag{1}$$

In order to use the difference in heat transfer to distinguish between the flow regimes, an initial temperature difference between the fluid and the surface has to exist. Since the amount of transferred heat is proportional to the temperature difference, an initially higher temperature difference leads to a higher thermal contrast between the flow regimes. Therefore typically either the air or the object is additionally heated or cooled in experiments within laboratory environments (de Luca et al., 1995). Note that active heating of the measurement object is sometimes not possible due to a limited access or a long working distance. However as long as the temperature difference between the surface and the fluid is high enough, the different surface temperatures of the flow regimes can be distinguished and measured without contact using thermography.

As an example, Fig. 1 shows a thermographic measurement of a rotor blade of a General Electric GE 1.5 sl wind turbine near the rotor blade root. With the rotor blade movement being downwards, the relative flow direction is upwards. Since the rotor blade is not actively heated and the temperature of the air cannot be influenced, the temperature difference between flow and surface relies on the amount of absorbed solar radiation by the rotor blade. As the turbulent flow regime has a higher friction and therefore a higher heat transfer coefficient than the laminar flow regime, the relatively cold air cools down the sun-heated rotor blade surface stronger in the area of the turbulent

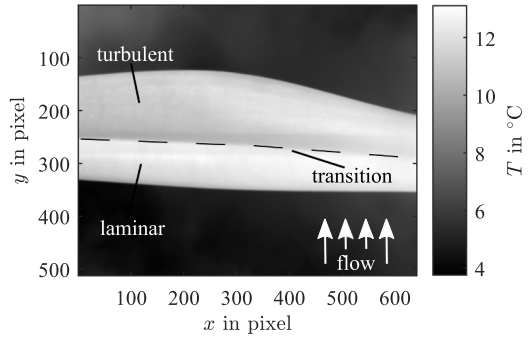

Fig. 1. Thermographic image of a rotor blade of a General Electric GE 1.5 sl wind turbine in operation with visible flow regimes. The blade is moving downwards, therefore the relative flow direction is upwards. The difference between laminar and turbulent flow is noticeable by a temperature drop in flow direction. The transition between the laminar and turbulent flow regime is marked with a dashed line.

flow compared with the area of the laminar flow. This can be seen by the brighter region at the bottom of the visible rotor blade in comparison with the top, cf. Fig. 1. The weather conditions at the time of the measurement were ideal due to sunshine and little cloud formation. This decreases the impact of the afore mentioned effects of the systematic temperature gradient and random temperature fluctuations compared to the difference in the spatial mean temperature. Therefore a pronounced temperature drop in flow direction at the border between the two flow regimes (cf. Fig. 1, $y \approx 250$ pixels) is noticeable. However, observing the surface area of the turbulent flow regime ($120\,\text{pixels} < y < 250\,\text{pixels}$) between $x = 200$ pixels and $x = 400$ pixels, a steady rise of temperature in flow direction can be noticed. This systematic temperature gradient exists due to the change in friction, effecting the inhomogeneity of the flow regime.

2.2. Non-Negative Matrix Factorization (NMF)

Non-negative matrix factorization (NMF) is closely related to other factorization methods like the principle component analysis (PCA) or vector quantization (VQ) and follows the same principle with additional constrains on the factorized matrices (Lee and Seung, 1999). All three methods follow the basic idea of approximating a given set of data by two matrices, reducing the number of dimensions without losing elementary information of the data set. A given $n \times m$ matrix V is approximated by a factorization of two matrices W and H of the form

$$V_{ij} \approx (WH)_{ij} = \sum_{k=1}^{r} W_{ik} H_{kj} \tag{2}$$

with $i = 1 \cdots n$, $j = 1 \cdots m$ and the dimensions of W and H being $n \times r$ and $r \times m$, respectively. To achieve a high dimension reduction, the rank r is chosen in a way that $r < \frac{mn}{m+n}$ is fulfilled. The optimal choice of r is problem dependant (Berry et al., 2007) and has to be found by trial and error with the goal to find the smallest possible value to achieve the highest compression of the informations given in the data. The matrices W and H are iteratively updated, following the alternating least square algorithm presented by Berry et al. (2007):

$W = W0$
for $i = 1$ to *maxIteration*
  Solve for H in matrix $W^T W H = W^T V$
  Set all negative elements in H to 0
  Solve for W in matrix $H H^T W^T = H V^T$
  Set all negative elements in W to 0
end

The initial starting point $W0$ is determined by multiple runs of the faster multiplicative update algorithm (Berry et al., 2007)

$W = rand(n, r)$
$H = rand(r, m)$
for $i = 1$ to *maxIteration*
  $H = H \cdot (W^T A) / (W^T W H + 10^{-9})$
  $W = W \cdot (A H) / (W H H^T + 10^{-9})$
end

whereas the 10^{-9} is used to avoid division by zero. After each iterative step the root-mean-square residual

$$K = \frac{\|V - WH\|_F}{\sqrt{n \cdot m}} \tag{3}$$

is calculated. $\|\cdot\|_F$ is the Frobenius norm defined for the elements a_{ij} of a given $n \times m$ matrix A by

$$\|A\|_F = \sqrt{\sum_{i=1}^{n} \sum_{j=1}^{m} |a_{ij}|^2}\,. \tag{4}$$

Both algorithms stop when the maximum number of iterations *maxIteration* is reached or if K is smaller than a specified maximum. Due to the existence of local minima at the minimization process of Eq. (2), W and H can reach different solutions when executing the NMF algorithm multiple times. Therefore the resulting NMF images can differ for each calculation, aggravating an automatic evaluation.

Since V contains the observed signals, it can be described as visible variables. The calculated matrix H can be described as hidden variables which co-activate a subset of new visible variables, the basis W, to approximate the original data V (Lee and Seung, 1999). Since the dimension r is much smaller than the dimensions of V, the size of the entire data content has been reduced while all elementary signal informations remain. A typical application of the NMF method due to the graphical presentation possibility is the parts-based representation of faces (Lee and Seung, 1999). While a set of images of faces is arranged column-wise in the matrix V, the matrix W and H are calculated following Eq. (2) and contain images with parts of faces and weighting factors, respectively. A linear combination of the images in W with the factors in one column of H results in an approximation of the original face image in V. In general the NMF can be used for all kinds of image applications where multiple images of similar objects containing the same features exist which differ only in the accentuation of these features.

The major difference between NMF and other feature extraction algorithms like PCA is the non-negativity constrain on the matrices W and H, still respecting Eq. (2) (Lee and Seung, 1999). Since PCA allows negative values in H, the base images contain information about all features of a face: This is possible because some of these base images can be combined subtractively, cancelling each other out. NMF does not allow these negative factors in the linear combination, hence no cancelling is possible. Therefore the base images contain only single features of a face which can be added or left out when reassembling a complete face image. This non-negativity constraint enables a more intuitive representation of the base images in W, in this example being parts of a real face, rather then abstract images which can be hardly interpreted individually.

2.3. Quantification of the distinguishability

In order to quantify the distinguishability of one flow regime compared to another flow regime, the temperature values of an evaluation region A within the first flow regime and an evaluation region B within the second flow regime are used to define the parameter

$$D_{A-B} = \frac{|\overline{T}_A - \overline{T}_B|}{s_A} \tag{5}$$

as the absolute difference of the mean temperatures, divided by the temperature standard deviation in the region of A. $\overline{T} = \frac{1}{n} \sum_{i=1}^{n} t_i$ is obtained from the n temperature values t_i in the considered flow area and s

is calculated as the spatial empirical standard deviation $s = \sqrt{\frac{1}{n-1}\sum_{i=1}^{n}(t_i - \overline{T})^2}$. The mean temperature difference is the desired signal and the standard deviation serves as a measure of the inhomogeneity of the flow regime. Note that the parameter defined by Eq. (5) is directed, meaning that D_{A-B} is not the same as D_{B-A}, and the different flow regimes are evaluated individually rather than quantifying their distinguishability as a pair.

In order to evaluate the impact of the systematic and random temperature inhomogeneity on the distinguishability of a flow regime pair separately, the effects are isolated from each other. The goal is to differentiate between the systematically influenced inhomogeneity (based on temperature gradients within the flow regimes or measurement artefacts) and the randomly influenced inhomogeneity (based on noise and spatial temperature fluctuations due to flow irregularities). This is done by quantifying the distinguishability on the bases of either the systematic or random part of the overall inhomogeneity. For extracting the information about the systematic inhomogeneity, the temperature field in the evaluation areas of the flow regimes is smoothed and afterwards subtracted from the unsmoothed temperature field in order to isolate the fluctuations. Next, the spatial standard deviation of the smoothed temperature field and the spatial standard deviation of the random temperature fluctuation field are calculated. For each standard deviation, the parameter D is determined separately according to Eq. (5), which enables a study of the effects of the systematic and random temperature inhomogeneity on the thermographic flow visualization. In order to cope with the different occurring flow regimes' systematic gradients, a cubic smoothing spline (de Boor, 2001) is used for the smoothing process as it prove to be robust towards their varieties. A specifically small smoothing parameter of $p = 1 \times 10^{-4}$ was chosen to mimic a low order polynomial fit while preserving the flexibility of a spline function. Since no generally applicable distinction between the systematic or random inhomogeneity exist and the goal is not to separate the signal from measurement noise, the decision of the smoothing parameter and hence the threshold of labelling an inhomogeneity as systematic or random is made by the author through experimenting with multiple temperature fields of different flow regimes. The definition of systematic and random therefore underlies the author's decision. This tends to be sufficient for the presented work, since the goal is a comparison of the measurement images and the following NMF evaluation and not a quantification of systematic and random effects individually as it would be, for instance, in a signal to noise separation task.

Fig. 2 (a) shows the temperature field of the evaluation area of the turbulent flow regime from the thermographic images used in this work (cf. Fig. 5 (a)). Note that the temperature shows a positive gradient in x-direction and has many random small fluctuations that can be explained by irregularities in the flow superimposed with random noise of the infrared camera. Fig. 2 (b) shows the same temperature field smoothed with the smoothing spline and hence just reflects the temperature gradient without the small fluctuations. By subtracting the field in (a) and (b), only these fluctuations remain as shown in Fig. 2 (c). Calculating the standard deviation (std) of the values in (b) results in a quantification of the temperature gradient while the calculation of the standard deviation of the pattern (c) results in the quantification of the random fluctuations. Both influences to the overall inhomogeneity of the temperature field T are separated to calculate the distinguishability parameter D in Eq. (5) for systematic and random temperature fluctuations, respectively.

In order to demonstrate the evaluation of the systematic and the random distinguishability parameter, a numerical example is considered. The presented temperature field A has a mean temperature of $\overline{T}_A = 12.12$ °C and the standard deviation of the systematic and random fluctuations amounts to $s_s = 0.117$ and $s_r = 0.041$, respectively. Assuming a mean temperature $\overline{T}_B = 11.87$ °C in another temperature field and applying Eq. (5), the quantification of the systematically influenced distinguishability is

$$D_s = \frac{|\overline{T}_A - \overline{T}_B|}{s_s} = \frac{|12.12\,°\text{C} - 11.87\,°\text{C}|}{0.117\,°\text{C}} = 52.1 \tag{6}$$

and the randomly influenced distinguishability is

$$D_r = \frac{|\overline{T}_A - \overline{T}_B|}{s_r} = \frac{|12.12\,°\text{C} - 11.87\,°\text{C}|}{0.041\,°\text{C}} = 6.1. \tag{7}$$

For this example, the distinguishability parameters show that the systematic inhomogeneity in the flow regime A in the form of a temperature gradient is the dominant influence on the distinguishability. Calculating the distinguishability parameters for the thermographic images as well as for the NMF results, an assessment of the NMF results regarding the possibly improved distinguishability between flow regime pairs based on a reduced systematically or randomly influenced inhomogeneity can be conducted.

To make a statement about the overall distinguishability between a pair of flow regimes, the commonly used contrast-to-noise ratio

$$CNR_{A,B} = \frac{(\overline{T}_A - \overline{T}_B)^2}{s_A^2 + s_B^2}. \tag{8}$$

is also defined.

3. Experimental setup

In order to investigate the potential of the presented data evaluation method, measurements at Deutsche WindGuard's Aeroacoustic Wind Tunnel (DWAA) in Bremerhaven, Germany and the German Aerospace Center (DLR) in Göttingen, Germany are conducted. To evaluate the distinguishability of different flow regimes, a flow measurement on a cylinder is carried out, because this geometry enables the coexistence of multiple flow phenomena on one single surface, cf. Section 3.1. To investigate the potential of the NMF evaluation method to visualize the expansion of the laminar-turbulent flow transition on an aerodynamic profiles, a flow measurement on a helicopter airfoil is presented in cf. Section 3.2.

3.1. Cylinder

The cylinder measurements are conducted at Deutsche WindGuard's DWAA wind tunnel. The aero-acoustic wind tunnel can be operated with a closed or open test section and reaches wind speeds of up to 100 m/s, resulting in Reynolds numbers of up to $Re = 6.0 \times 10^6$, while achieving a turbulence intensity of less than 0.3 %. Inside the closed test section aerodynamic models with a chord length of up to 0.9 m can be measured between two turntables at the ceiling and the floor of the test

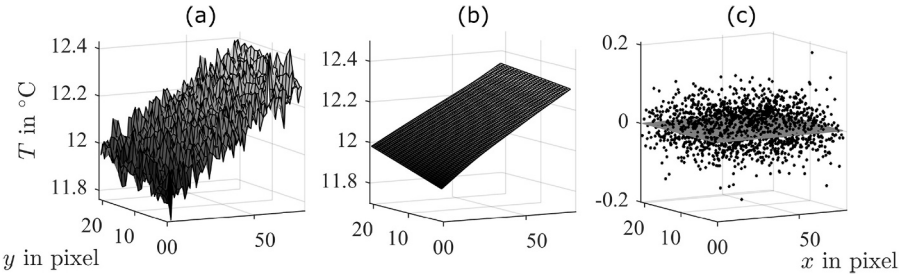

Fig. 2. (a) Example temperature pattern T with a systematic temperature gradient superimposed with random fluctuations. (b) Smoothed temperature pattern of T, representing the temperature gradient without fluctuations (standard deviation: 0.117 °C). (c) Random temperature fluctuations of the T, calculated by subtracting the pattern in (a) from the pattern in (b) (standard deviation: 0.041 °C.)

section. The turntables allow an adjustment of the angle of attack as well as a measurement of the total wind forces, i.e. the lift and drag, acting on the model. Additional pressure sensors on the side of the test section and connected to pressure taps on the model surface measure the lift indirectly.

To fundamentally investigate the feasibility of the contrast enhancing evaluation method presented in this article, a cylinder is chosen as the measurement object. With a diameter of 160 mm and a wind speed of 50 m/s, a supercritical flow can be achieved which allows the occurrence of different flow regimes on the surface at a Reynolds number of $Re = 5.1 \times 10^5$. This setup allows a laminar flow regime, a laminar separation bubble, a turbulent flow regime and a flow separation regime to be observed simultaneously.

The cylinder is mounted vertically between the turntables in the middle of the closed test section of the wind tunnel. The material used is polyoxymethylene, an easy to machine material with optical and thermal properties suitable for thermographic flow measurements without the necessity of an additional surface preparation. It has a high emissivity, a low heat capacity and conduction and a surface roughness that minimizes the reflection but doesn't disturb the flow. Fig. 3 illustrates the experimental setup. In order to check the position of the different measured flow regimes, an oil flow visualisation is carried out before the thermographic measurements. The cylinder surface is covered with a thin layer of a daylight fluorescent silicone oil mix. An optical digital single-lens reflex camera takes an image every 30 s to allow an identification of the changing oil pattern and hence the development of the different flow regimes.

For the thermographic imaging of the cylinder surface a thermographic camera, model *ImageIR 8300* from the manufacturer *InfraTec*, is used. The actively cooled InSb focal plane array works with a global shutter (snap-shot detector) and has a pixel size of 15 µm. At a full-frame resolution of 640 × 512 pixels the maximum frame rate is 100 Hz. The sensitivity is between 2 to 5 µm and the camera has a noise equivalent temperature difference (NETD) of less than 25 mK @ 30 °C. The dynamic range is 14 bit and the integration time can be selected between 1 and 20000 µs, whereby it is set to 1600 µs for the presented measurement. The camera is positioned on the side of the wind tunnel test section, facing the cylinder through a CaF_2 (calcium fluoride) window with a transmission of over 90 % for a wavelength between 2 and 5 µm. In order to maximize the optical resolution the thermography camera is equipped with a 100 mm telephoto lens with an angular aperture of, 4, 4 ° × 5, 5 °. At the viewing distance of 1.75 m, the field of view of 0.15 mrad results in a geometric resolution of 0.26 mm on the object surface represented by one pixel.

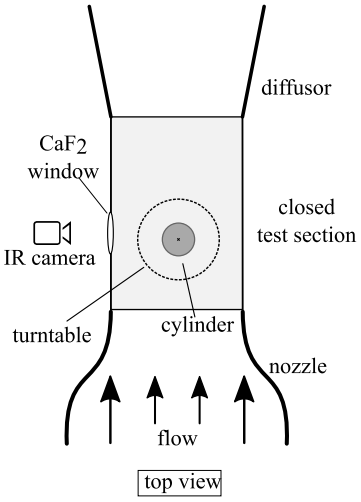

Fig. 3. The cylinder with a diameter of $d = 160$ mm and a span of 1250 mm in the closed test section of the Deutsche WindGuard's aeroacoustic wind tunnel in Bremerhaven, Germany at a wind speed of $v_\infty = 50$ m/s, $Re = 5.1 \times 10^5$.

After exporting the image stream from the thermographic camera with the manufacturer's software, the image series is integrated into Matlab for subsequent processing. Due to the surface curvature and the viewing angle not normal to the flow direction the surface is deformed in the image. The direction of view and the angle of aperture of the telephoto lens as well as the object geometry are taken into account to correct the distortion. As a result of the curved object geometry, the areas with different viewing angles appear to have a non-uniform temperature distribution. Note that this change in captured radiation intensity is caused by the directional emissivity of the surface and remains uncorrected. At the moment of image acquisition no active heating of the cylinder surface was used, resulting in a temperature range on the surface of only 1 K. Due to friction in the wind tunnel the flow temperature is higher than the cylinder surface temperature.

3.2. Helicopter airfoil

The flow measurements of the helicopter airfoil model DSA-9A are conducted in the wind tunnel of the DLR. The airfoil model has a chord length of 0.3 m, a span length of 0.997 m and is positioned horizontally in the open test section of the "one-meter wind tunnel" in Goettingen. The sides of the airfoil model, crosswise to the direction of flow, are enclosed with two plates to ensure a two-dimensional flow. The wind speed is 50 m/s, resulting in a Reynolds number of $Re = 1.0 \times 10^6$. The angle of attack α is 0°, measured by laser triangulation sensors. The thermographic images are acquired with a thermographic camera, model *SC7750L*, from the manufacturer *FLIR* with a Mercury Cadmium Telluride detector and an internal Sterling cooler. The manufacturer specifies a NETD of less than 30 mK @ 30 °C. It is sensitive in a range of 8.0 to 9.4 µm and has a maximum resolution of 640 × 512 pixels at an acquisition frequency of up to 115 Hz, though it is set to 99.98 Hz for the presented measurement. The reason the frequency is not set to exactly 100 Hz or the maximum amount is that the same experimental setup is used to conduct dynamic measurements with a high frequency pitching airfoil for stall detection. To realise a de-synchronization between camera and the pitching movement, the camera acquisition is set slightly off to the integral multiples of the model's pitching frequencies (Wolf et al., 2019). The integration time of the camera is set to 190 µs. The camera is mounted 2 m above the airfoil, facing downwards with a 50 mm focal lens with an angular aperture of 11.7° × 9.4° (cf. Fig. 4).

In order to achieve a high thermal contrast between the flow regimes, active heating of the surface is realized by a spot light next to the camera. With a power output of up to 1500 W a temperature difference between the free flow and the model object of 5 to 6 K can be achieved.

4. Measurement results

4.1. Cylinder

The acquired thermographic images and therefore also the resulting images of the NMF algorithm are rectified to display the three dimensional surface of the cylinder in the two dimensional image plane and the surface areas are allocated to the angular values between $\phi = 0°$ to $\phi = 180°$ around the cylinder, cf. Fig. 5. The stagnation point is at $\phi = 0°$, resulting in a flow direction from left to right in the image plane. The surface area at the leading edge between $\phi = 0°$ and $\phi \approx 22°$ and trailing edge at $\phi \geq 170°$ is strongly affected by the reflection of daylight due to the curvature of the cylinder and is not suitable for an evaluation. The images have a resolution of 640 × 39 pixels. Instead of comparing the NMF evaluation results to one out of 6000 thermographic images taken, the comparison takes place between the NMF images and the arithmetic mean of the time series shown in Fig. 5 (a). If a series of N images is considered, the standard deviation of the noise in the mean temperature image reduced by the factor $\frac{1}{\sqrt{N}}$. Therefore, the mean image should be used for comparison of random fluctuations if

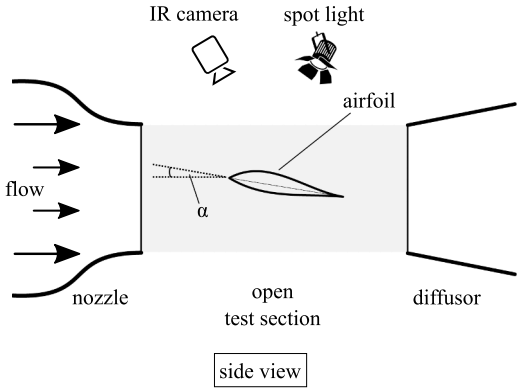

Fig. 4. The helicopter airfoil in the open test section of the DLR's wind tunnel in Göttingen, Germany. Wind speed $V_\infty = 50$ m/s, $Re = 1 \times 10^6$ at an angle of attack $\alpha = 0°$. (schematic representation)

multiple images exist. The boundaries of the flow regimes are indicated by a white dashed line. The exact dimensions of the flow regimes are extracted from the optical oil film measurement as a reference, depicted in Fig. 6. The experiment was conducted at a Reynolds number of $Re = 5.1 \times 10^5$ and the accumulation of the oil film detected with a digital single-lens reflex (DSLR) camera, as presented in Dollinger et al. (2018a). The two distinctive bright lines due to an accumulation of oil indicate the position of the laminar separation and the turbulent separation, at $\phi_{ls} = 102°$ and $\phi_{ts} = 140°$, respectively. The black line at $\phi = 117°$ is the position of the flow reattachment ϕ_r and the beginning of the turbulent flow regime.

Beside the high reflective areas at the leading and trailing edge, the surface temperature pattern of the flow regimes in the mean image Fig. 5 (a) can be explained by the local heat transfer. The laminar (L) flow regime has a relatively low friction coefficient, continuously increasing in flow direction (Schlichting, 1979). Between approximately $\phi = 80°$ and $\phi = 105°$ the reflection of the IR camera detector creates an artefact superimposing the surface temperature, resulting in a temperature gradient in the laminar (L) flow regime. After the laminar separation at $\phi_{ls} = 102°$, the laminar-turbulent transition takes place over the laminar separation bubble. Due to the self containment of the separation bubble (LS), heat exchange in this area is low, again resulting in a low surface temperature. After the reattachment of the laminar separation bubble at $\phi_r = 117°$, the turbulent flow (T) is characterized by a continuously increasing friction between the flow and the surface, resulting in a higher temperature compared to the laminar flow regime. At $\phi_{ts} = 140°$ the turbulent flow separates. In contrast to laminar and turbulent flow, there is no steep surface temperature change between turbulent and turbulent separated flow (TS), although the type of flow changes abruptly. The reason for this non-existing temperature step is the increasing friction coefficient in the turbulent flow that changes to a constant state as soon as the flow separates (de Luca et al., 1990). Therefore the thermal contrast between the turbulent and separated flow regime in the border area between them is small and obscures the distinguishability.

Because of the non-deterministic solution of the NMF, the algorithm

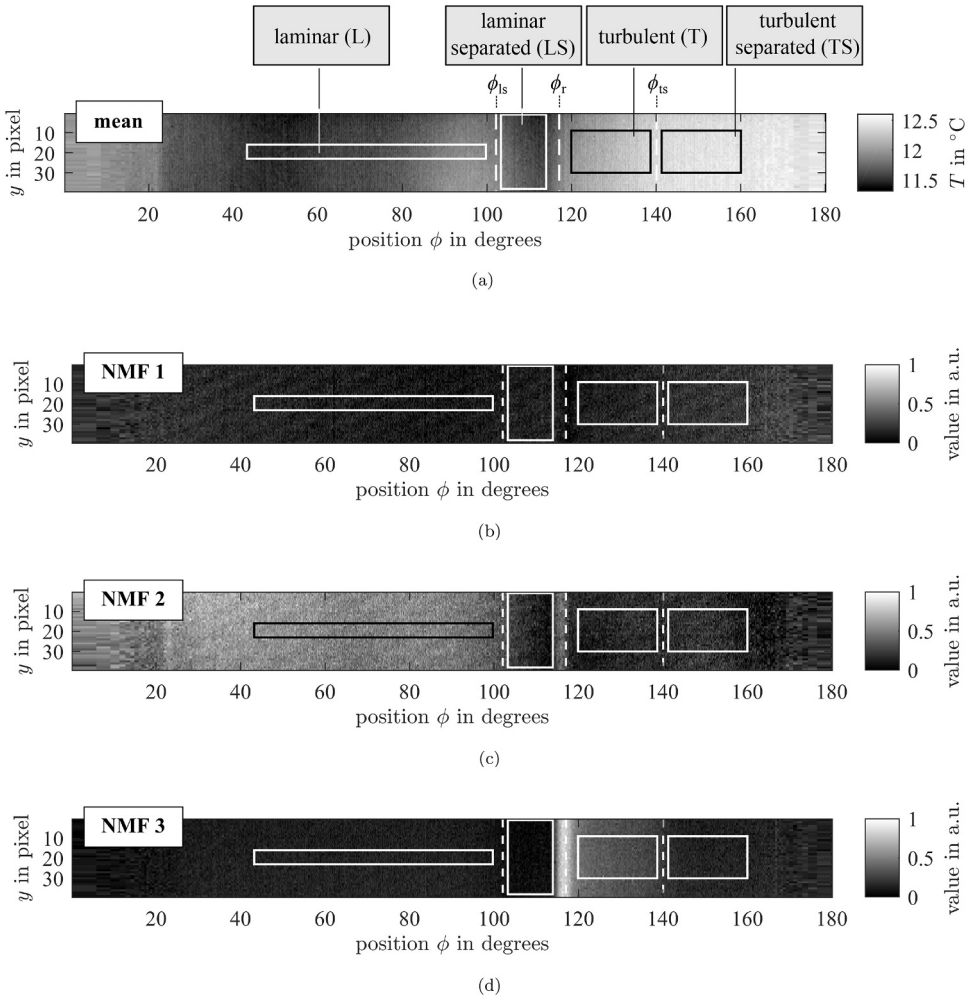

Fig. 5. Arithmetic mean image and the three selected NMF images with the highest distinguishability between flow regimes. Flow direction from left to right. (a) The arithmetic mean of the time series. (b)-(d) NMF images.

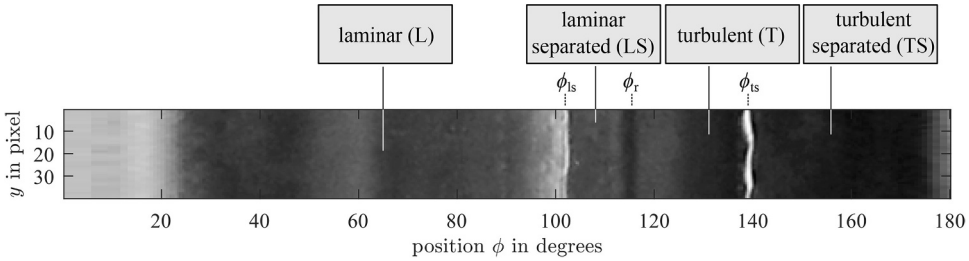

Fig. 6. Oil film flow visualization image of the cylinder at a Reynolds number of $Re = 5.1 \times 10^5$ with the flow direction from left to right. The oil pattern enables a distinction of the flow regimes, separated by the two vertical bright lines (separations) and the single vertical dark line (reattachment). The laminar flow starts at the leading edge $\phi = 0°$ until the flow separates at $\phi_{ls} = 102°$ in form of a laminar separation bubble. The turbulent flow regime starts at the flow reattachment position at $\phi_r = 117°$ and separates at $\phi_{ts} = 140°$.

is executed multiple times and each resulting set of images is evaluated concerning the distinguishability between flow regimes. The NMF images presented in this paper are then selected from the one NMF solution with the highest increase in the distinguishability parameter D, cf. (5). The NMF algorithm converges for the given images of the time series to the dimension parameter $r = 10$, resulting in ten images for each NMF solution. Fig. 7 shows the arithmetic mean image of the time series and all ten NMF images. These images are extracted from the matrix W of the factorization presented in Section 2.2. The factors in the matrix H are not regarded in this evaluation. As a result, the signal information of the time series is divided into various patterns with different parts of the signal emphasized in each image. In most images, for example NMF 2, NMF 3, NMF 6, different flow regimes are emphasized, in other images like NMF 6 and NMF 9 the reflection at the leading and trailing edge have the highest amplitude. Again, other NMF images offer almost no distinguishability between the flow regimes as they seem to contain only random noise.

Observing the NMF images in Fig. 7, it seems that a different flow regimes are emphasized in each image. This supports the initial hypothesis that the NMF actually extracts the different signals of the flow regimes of the time series and can represent them in different feature images. However, the first image, NMF 1, is an example of a NMF result without any emphasized flow regime. This indicates, that there is globally distributed noise recognized as a feature. NMF 2 seems to have an emphasized laminar flow, visible through the higher amplitude between $\phi = 20°$ and $\phi = 102°$. The laminar separation bubble, as well as the turbulent and turbulent separated flow show an almost homogeneous intensity pattern. This offers the possibility of a high distinguishability between the laminar flow and the turbulent flow. In NMF 3, the turbulent flow between $\phi = 118°$ and $\phi = 139°$ is empathized compared to the other flow regimes. However, the most highlighted area is the reattachment at $\phi \approx 117°$.

For further investigation, the three best NMF images regarding their distinguishability between the flow regimes, labelled NMF 1 to NMF 3, are chosen and shown in Fig. 5 (b) - (d) below the mean image of the time series. Since the factorization method splits the signal informations of the input images into multiple images, the intensity values of the NMF images do not have any real world relation and are refereed to as with an amplitude in an arbitrary unit. For each flow regime an evaluation area is defined in order to quantify the random and systematic influence on the distinguishability and the resulting CNR, cf. Section 2.3. For a comparison of the standard deviations and mean temperatures between the areas and also considering the temperature gradient, the areas have the most possible width in flow direction while containing the same amount of pixels, being 1665 pixels per area.

In the following the parameter D for the distinguishability influenced by the random flow inhomogeneity and the systematic flow inhomogeneity for each pair of flow regimes is presented in order to evaluate the effects individually. Additionally, the contrast-to-noise ratio CNR is discussed. In order to evaluate the improvement through the NMF method, the values of the arithmetic mean image are

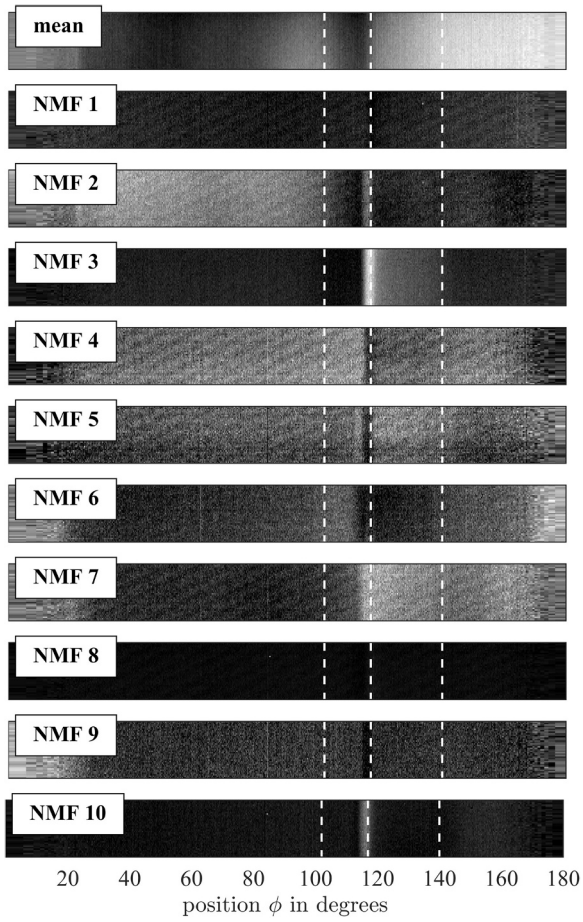

Fig. 7. Arithmetic mean image of the time series and NMF images of the NMF solution with the highest distinguishability between flow regimes of the cylinder experiment.

considered as a reference.

The calculated distinguishability parameter D for the random temperature inhomogeneity of the flow regimes for the evaluation areas depicted in Fig. 5 are summarized in Table 1. Next to the columns listing the parameters D for each image, the last column shows the improvement between the mean image and the NMF result with the highest value of D. The distinguishability only improves between the laminar and the laminar separated flow regimes in NMF 2 (bold values) and NMF 3. The resulting distinguishability increases compared to the value in the mean image by a factor 21 and 25 for the laminar and the laminar separated flow regime, respectively. For every other NMF image and pair of flow regimes, no increase for D is registered. Since the distinguishability based on the random temperature fluctuations within the flow regimes does not increase, but rather decrease in the NMF

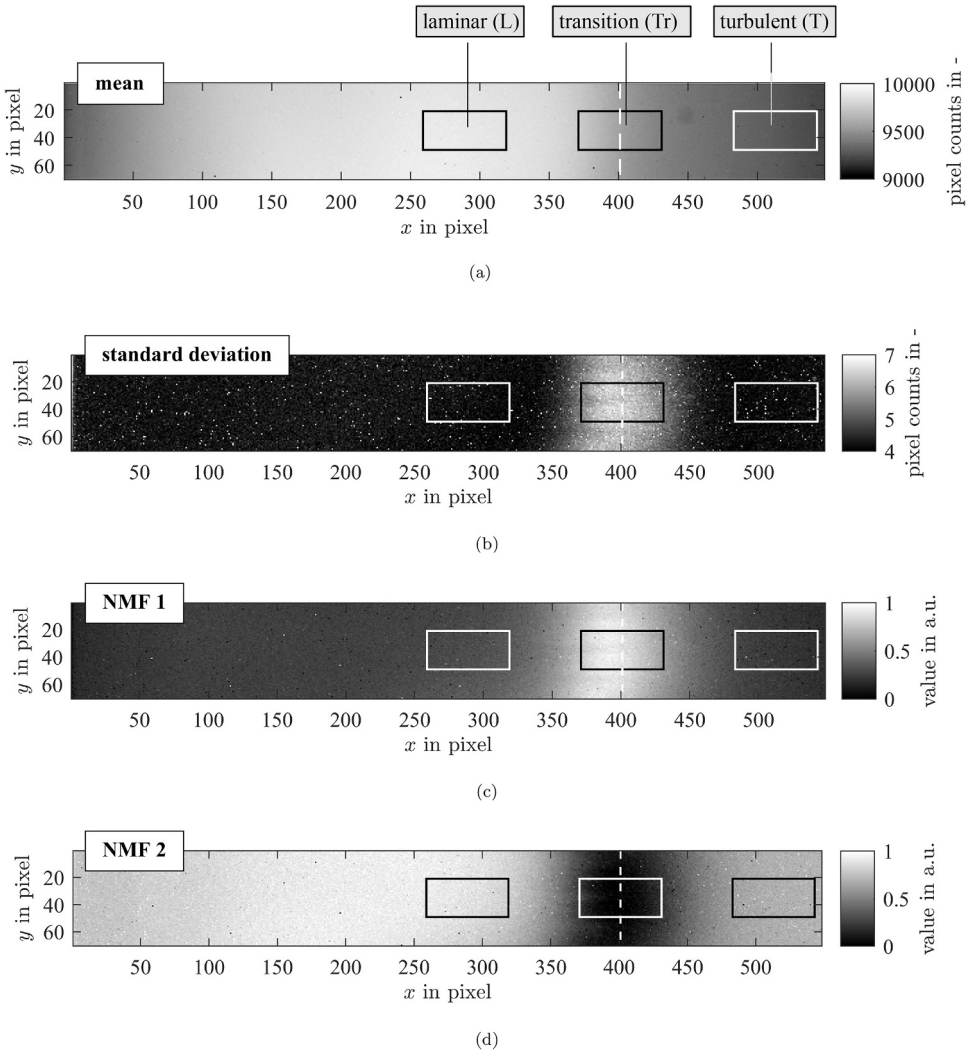

Fig. 8. Helicopter airfoil measurement. Flow direction from left to right. (a) Arithmetic mean image of the time series. (b) Standard deviation and (c)-(d) NMF images.

results, the amount of random fluctuations is not lowered through the evaluations process. Hence the randomly influenced temperature inhomogeneities in the flow regimes do not decrease.

The distinguishability parameter D for the systematic temperature inhomogeneity in the different flow regimes are listed in Table 2. In contrast to the random inhomogeneity, an increase of the distinguishability influenced by the systematic temperature inhomogeneity is achieved for every flow regime (bold values), within the selected NMF results. Except for the comparison of the turbulent and laminar flow regime, every pair of flow regimes has the maximum increase in the NMF 3 image. For the other flow regimes, the improvement of D in the NMF 3 image ranges from 17 % to 495 %. An increase of D of 209 % for the turbulent flow regime compared with the laminar flow regime can instead be found in NMF 2. For the comparison of the laminar and the

Table 1
Distinguishability D (cf. (5)) between flow regimes in the cylinder experiment based on the influence of the random inhomogeneity. Calculated on the basis of the mean temperature difference $|\overline{T}_A - \overline{T}_B|$, normalized to the random standard deviation s of the random temperature fluctuations in the flow regime A. The last column shows the maximum increase relative to the value in the mean image.

Distinguishability (due to random inhomogeneity) D_{A-B}						
Flow regime A	Flow regime B	Mean	NMF 1	NMF 2	NMF 3	Max. improvement
laminar (L)	laminar separated (LS)	**0.2**	0.1	**4.6**	2.0	2180%
	turbulent (T)	**13.1**	0.4	4.7	5.2	–
laminar-separated (LS)	laminar (L)	**0.2**	0.1	**4.8**	2.1	2583%
	turbulent (T)	**11.9**	0.3	0.1	7.4	–
turbulent (T)	laminar separated (LS)	**11.8**	0.3	0.1	7.1	–
	turbulent separated (TS)	**6.7**	1.1	0.3	4.7	–
	laminar (L)	**12.0**	0.4	4.8	5.1	–
turbulent separated (TS)	turbulent (T)	**6.7**	1.2	0.3	4.6	–

Table 2
Distinguishability D (cf. (5)) between flow regimes in the cylinder experiment based on the influence of the systematic inhomogeneity. Calculated on the basis of the mean temperature difference $|\overline{T}_A - \overline{T}_B|$, normalized to the systematic standard deviation s of the systematic temperature gradients in the flow regime A. The last column shows the maximum increase relative to the value in the mean image.

Distinguishability (due to systematic inhomogeneity) D_{A-B}						
Flow regime A	Flow regime B	Mean	NMF 1	NMF 2	NMF 3	Max. improvement
laminar (L)	laminar separated (LS)	**0.1**	0.4	**7.5**	**8.1**	16160%
	turbulent (T)	**3.5**	1.2	**7.7**	**21.0**	495%
laminar separated (LS)	laminar (L)	**0.1**	0.9	**5.0**	**7.4**	10500%
	turbulent (T)	**4.8**	1.6	0.1	**26.6**	450%
turbulent (T)	laminar separated (LS)	**4.2**	0.7	0.4	**5.7**	37%
	turbulent separated (TS)	**2.4**	3.1	0.9	**3.8**	60%
	laminar (L)	**4.2**	1.1	**13.1**	4.1	209%
turbulent separated (TS)	turbulent (T)	**9.8**	6.3	0.9	**11.4**	17%

laminar separated flow regimes an increase of factor 105 and 161 is achieved. The overall increase in D implies a significant reduction of the effect of the systematic temperature inhomogeneity on the thermographic flow visualization by the NMF approach. Particularly the error from the systematic inhomogeneity in the laminar flow regime is reduced drastically, which is obvious by comparing the mean temperature image with the NMF images in Fig. 5. This is in agreement with the visual evaluation of the NMF images showing a reduced temperature gradient in flow direction.

As a result of the increased distinguishability in NMF 3 due to a reduced effect of the systematic temperature inhomogeneity in most flow regimes, the CNR value is increased for every pair of consecutive flow regimes including the laminar-turbulent flow regime pair (Table 3). The CNR values increase by 36 % for the turbulent and turbulent separated flow regime pair, 63 % for laminar separated-turbulent and 32 % for the laminar - turbulent flow regime pair. The CNR between the laminar and laminar separated flow regime even increases from 0.1 to 2.0. Hence, the NMF approach enables an increase of the distinguishability between flow regimes by reducing the systematic temperature gradients and therefore increasing the CNR.

4.2. Helicopter airfoil

Fig. 8 (a) shows the arithmetic mean image of the time series containing 1119 single measurements. The flow direction is from left to right with a laminar (L) to turbulent flow (T) transition (Tr) at $x = 401$ pixels, marked with a white dashed line. The position of the flow transition was defined by the maximum temperature gradient of the column-wise averaged image in x-direction. As mentioned before, it needs to be noted, that the transition does not exist in an infinitesimally small area, but rather has a spatial expansion in flow direction (Richter et al., 2015). This way a clear separation of areas which contain only information about the laminar and turbulent flow regime is difficult. For the following evaluation three areas are defined as shown in Fig. 8: One for the laminar flow regime and one for each the transition and the turbulent flow regimes. This way, the distinguishability between the flow regimes and the transition area can be quantified.

Fig. 8 (b) shows the standard deviation for every pixel in the time series of images. Fig. 8 (c) and (d) shows the NMF images. After multiple evaluations of the algorithm, the NMF solution with the images with the highest distinguishability between the flow regimes and the transition area was selected. It is noticeable that the area in which the transition expands is strongly emphasized in the NMF 1 image. This can be compared to the emphasized reattachment in NMF 3 in the previous results of the cylinder measurement, since this can also be traced back to strong temperature fluctuations. In NMF 2 of the airfoil measurement the same transition area is negatively emphasized compared with the other evaluation areas but the distinguishability between the flow regimes seems to be even higher than in NMF 1.

Observing the standard deviation image concludes a similar result as the NMF 1 image. However, an investigation of the distinguishability D reveals no increase, but rather a decrease in the randomly influenced distinguishability between the flow regimes and the transition area took place. Table 4 lists the values for the distinguishability parameter D influenced by the random inhomogeneity of the flow regimes. It can be noted, that no increase in D is achieved through either the calculation of the standard deviation nor the NMF algorithm. However the distinguishability is higher in both NMF images compared to the image of the standard deviation. This can be explained by the noisy standard deviation image, due to a strong non-uniformity in the gradient and zero-offset of individual pixels. Even though a two-point calibration before the measurement is conducted, some pixels are measuring in a different

Table 3
CNR between flow regimes in the cylinder experiment. The second column contains the average CNR of all thermographic images in the time series. The third column contains the CNR in the arithmetic mean image. The last column shows the maximum increase in CNR relative to the value in the mean image. The first three rows are the transitions of consecutive flow regimes in flow direction. Basis of the evaluation are the areas shown in Fig. 5.

	CNR single img	CNR **mean img**	CNR NMF 1	CNR NMF 2	CNR NMF 3	Max. improvement
laminar (L) / laminar separated (LS)	0.1	**0.1**	0.1	**6.7**	**2.0**	332400%
laminar separated (LS) / turbulent (T)	8.3	**8.7**	0.1	0.1	**14.1**	63%
turbulent (T) / turbulent separated (TS)	3.5	**4.2**	0.6	0.1	**5.7**	36%
laminar (L) / turbulent (T)	6.5	**6.7**	0.1	**8.8**	**7.3**	32%

Table 4
Distinguishability D (cf. (5)) between flow regimes in the airfoil experiment based on the influence of the random inhomogeneity. Calculated on the basis of the mean temperature difference $|\overline{T}_A - \overline{T}_B|$, normalized to the random standard deviation s of the random temperature fluctuations in the flow regime A. The last column shows the maximum increase relative to the value in the mean image.

Distinguishability (due to random inhomogeneity) D_{A-B}						
Eval. area A	Eval. area B	Mean	std	NMF 1	NMF 2	Max. improvement
laminar (T)	transition (Tr)	**32.7**	3.5	17.6	20.5	–
	turbulent (L)	**62.4**	0.1	3.0	5.1	–
transition (Tr)	laminar (T)	**33.8**	5.2	14.2	17.7	–
	turbulent (L)	**30.7**	5.3	16.6	13.3	–
turbulent (L)	laminar (T)	**72.0**	0.1	2.5	4.4	–
	transition (Tr)	**34.3**	2.1	16.9	13.2	–

Table 5
Distinguishability D (cf. (5)) between flow regimes in the airfoil experiment based on the influence of the systematic inhomogeneity. Calculated on the basis of the mean temperature difference $|\overline{T}_A - \overline{T}_B|$, normalized to the systematic standard deviation s of the systematic temperature gradients in the flow regime A. The last column shows the maximum increase relative to the value in the mean image.

Distinguishability (due to systematic inhomogeneity) D_{A-B}						
Eval. area A	Eval. area B	mean	std	NMF 1	NMF 2	Max. im- provement
laminar (T)	transition (Tr)	**27.0**	24.4	24.3	22.8	-
	turbulent (L)	**51.5**	0.4	4.2	5.7	-
transition (Tr)	laminar (T)	**3.3**	7.7	6.0	**16.2**	385%
	turbulent (L)	**3.0**	7.8	7.1	**12.1**	301%
turbulent (L)	laminar (T)	**18.4**	0.8	3.7	11.3	-
	transition (Tr)	**8.8**	**47.1**	25.5	33.8	538%

sensitivity region compared to other ones. These false values result in a high random inhomogeneity in the evaluation areas of the standard deviation image, while the feature extraction of the NMF is hardly influenced and therefore does not result in the same high random inhomogeneity in the NMF images. This solution reveals that the NMF is not capable of reducing any random inhomogeneity that would increase the distinguishability, however has higher values for D compared with the standard deviation of the time series.

An investigation of Table 5 reveals that the distinguishability between the transition and the two flow regimes could be increased by reducing the systematic inhomogeneity of the transition area in the NMF 2 image. Compared with the turbulent flow regime, the distinguishability of the transition was increased from $D_{Tr-L} = 3.0$ to $D_{Tr-L} = 12.1$, an improvement of 301 %. Compared to the laminar flow regime it increased even higher from $D_{Tr-T} = 3.3$ to $D_{Tr-T} = 16.2$, an improvement of 385 %. Obviously, the NMF algorithm is capable of reducing the temperature gradient in the transition area, increasing it's distinguishability from the flow regimes.

Table 6 reveals the increase of the CNR value between the laminar flow regime and the turbulent flow regime compared to the transition area of 562 % and 418 % in the NMF 2 image, respectively. This can be traced back to the reduction of the systematic inhomogeneity of the flow regimes.

The results show the potential of the NMF to extract additional information about the flow transition phenomena. The spatial expansion of the transition can hardly be detected in the arithmetic mean image but was visible as a dominant feature in the NMF 2 result. While the mean image uses the advantage of averaging in order to reduce the impact of outliers and noise, the standard deviation image is capable of visualizing the area of the transition. With applying the NMF it is possible to use both advantages because the area of the transition can be visualized while the noise and impact of outliers is smaller than in the standard deviation image. The extraction of the information about the transition expansion enables a correct positioning of the evaluation areas representing only flow regimes or the transition.

5. Conclusion and outlook

Non-negative matrix factorization was applied to a time series of thermographic images for flow visualization. By evaluating the temperature inhomogeneity of a flow regime compared to the difference in

Table 6
CNR between flow regimes in the airfoil experiment. The second column contains the CNR in the arithmetic mean image. The third column the values of the temporal standard deviation. The last column shows the maximum increase in CNR relative to the value in the mean image. The first two rows are the comparison of the flow regime areas with the transition area. The last row is the comparison between the flow regimes. Basis of the evaluation are the areas shown in Fig. 8.

	CNR	CNR	CNR	CNR	Max. improvement
	Mean	std	NMF 1	NMF 2	
laminar (T) / transition (Tr)	**10.7**	6.7	23.6	**70.8**	562%
turbulent (L) / transition (Tr)	**8.0**	3.5	31.0	**41.6**	418%
laminar (L) / turbulent (T)	264.0	0.1	2.5	7.7	–

spatial mean temperature to another flow regime, the distinguishability was quantified. The systematic influences on the temperature inhomogeneity of the flow regimes is reduced by the NMF, increasing the distinguishability of every flow regime pair. The reduction of the systematic temperature gradient increases the contrast-to-noise ratio between every consecutive flow regime pair. At the same time a reduction of the random inhomogeneity could not be achieved.

The evaluation of the helicopter airfoil flow has shown NMF has furthered the potential to visualize the spatial expansion of the laminar-turbulent transition region. This information extraction is difficult to realize in a single image or the arithmetic mean image. Here, the systematic temperature gradient within the transition area was reduced while the difference in mean temperature was increased. The result is an increase of the distinguishability between the transition region and the adjoining flow regimes while the impact of noise and outliers was minimized. As a result, the contrast-to-noise ratio between the transition area and the laminar and turbulent flow regime was increased.

To achieve the best results with NMF for increasing the CNR, the algorithm has to be executed multiple times. The minimization process of the iterative factorization method can reach a local minimum and therefore return different results in every execution of the algorithm. This disqualifies the method to be used in a fast and automatic evaluation, due to the non-deterministic results. Furthermore, the decision of which NMF result is presented as the optimal one is in the present work based on the evaluation of the different flow regimes' distinguishability. Since the areas of the different flow regimes must be known in this approach, NMF evaluation as presented here is less suitable for identifying the different flow regimes, but for increasing their distinguishability. Another limitation of the method is the necessity of acquiring a time series to be used with the NMF. In order to obtain sufficient signal information for the algorithm, multiple images of the static flow distribution are required, which prolongs the measurement time and hinders the measurement in a non-static environment.

Nonetheless, the presented method offers the possibility to reduce the systematic effects of inhomogeneous temperature patterns within the flow regimes. Especially in measurements with low initial thermal contrast, the NMF can be used to improve the distinguishability. Furthermore, the non-instantaneous transition process between the laminar and turbulent flow regime can be emphasized to improve the separation of the flow regimes before and after the transition and the transition region.

The present work merely covers a first evaluation of the NMF evaluation approach of the thermographic images and should trigger future studies. To understand the limits of NMF regarding the minimum amount of individual measurements necessary or the choice of optimal parameters including the dimension r of the matrices W and H as well as the tolerance of the residual K are goals to achieve an optimal factorization, especially regarding the non-deterministic of the algorithm. Other aspects that need to be investigated are the influence of different frequencies of the image acquisition and how temporal resolved temperature fluctuations impact the solution. Additionally, a combination of different NMF images should be considered for further increasing the flow image contrast.

CRediT authorship contribution statement

Daniel Gleichauf: Writing - original draft, Conceptualization, Methodology, Software, Writing - review & editing. **Christoph Dollinger:** Conceptualization, Investigation, Writing - review & editing. **Nicholas Balaresque:** Investigation, Writing - review & editing. **Anthony D. Gardner:** Investigation, Writing - review & editing. **Michael Sorg:** Supervision, Writing - review & editing. **Andreas Fischer:** Supervision, Writing - review & editing.

Declaration of Competing Interest

The authors declare that there are no conflicts of interest.

Acknowledgements

The authors gratefully acknowledge the financial support of the Deutsche Forschungsgemeinschaft (DFG project number FI 1989/5-1) and the support by the Institute of Aerodynamics and Flow Technology - Helicopters of the German Aerospace Center (DLR) and the Deutsche WindGuard for the experimental data and InfraTec for the technical support during the experiments.

References

Bæk, P., Fuglsang, P., 2009. Experimental detection of transition on wind turbine airfoils. Proceedings of the European Wind Energy Conference and Exhibition. pp. 1628–1652.

Berry, M.W., Browne, M., Langville, A.N., Pauca, V.P., Plemmons, R.J., 2007. Algorithms and applications for approximate nonnegative matrix factorization. Comput. Stat. Data Anal. 52 (1), 155–173. https://doi.org/10.1016/j.csda.2006.11.006.

Corten, G.P., Veldkamp, H.F., 2001. Insects can halve wind-turbine power. Nature 412, 41.

Crawford, B.K., Duncan, G.T., West, D.E., Saric, W.S., 2013. Laminar-turbulent boundary layer transition imaging using IR thermography. Opt. Photon. J. 3 (3), 233–239. https://doi.org/10.4236/opj.2013.33038.

de Boor, C., 2001. A Practical Guide to Splines. Springer.

de Luca, L., Carlomagno, G.M., Buresti, G., 1990. Boundary layer diagnostics by means of an infrared scanning radiometer. Exp. Fluid 9 (3), 121–128. https://doi.org/10.1007/BF00187411.

de Luca, L., Guglieri, G., Cardone, G., Carlomagno, G.M., 1995. Experimental analysis of surface flow on a delta wing by infrared thermography. AIAA J. 33 (8), 1510–1512. https://doi.org/10.2514/3.12574.

Dollinger, C., Balaresque, N., Gaudern, N., Gleichauf, D., Sorg, M., Fischer, A., 2019. IR thermographic flow visualization for the quantification of boundary layer flow disturbances due to the leading edge condition. Renew. Energy 138, 709–721. https://doi.org/10.1016/j.renene.2019.01.116.

Dollinger, C., Balaresque, N., Sorg, M., Fischer, A., 2018. IR thermographic visualization of flow separation in applications with low thermal contrast. Infrared Phys. Technol. 88, 254–264. https://doi.org/10.1016/j.infrared.2017.12.001.

Dollinger, C., Sorg, M., Balaresque, N., Fischer, A., 2018. Measurement uncertainty of IR thermographic flow visualization measurements for transition detection on wind turbines in operation. Exp. Therm. Fluid Sci. 97, 279–289. https://doi.org/10.1016/j.expthermflusci.2018.04.025.

Gardner, A.D., Wolf, C.C., Raffel, M., 2016. A new method of dynamic and static stall detection using infrared thermography. Exp. Fluid 57 (9), 149. https://doi.org/10.1007/s00348-016-2235-4.

Gartenberg, E., Johnson, W.G., Wright, R.E., Carraway, D.L., Johnson, C.B., 1992. Boundary-layer transition-detection in a cryogenic wind tunnel using infrared imaging. AIAA J. 30 (2), 444–446. https://doi.org/10.2514/3.10936.

Gartenberg, E., Roberts, A.S., 1991. Airfoil transition and separation studies using an infrared imaging system. J. Aircraft 28 (4), 225–230. https://doi.org/10.2514/3.46016.

Gartenberg, E., Roberts, A.S., McRee, G.J., 1989. Infrared imaging and tufts studies of boundary layer flow regimes on a NACA 0012 airfoil. International Congress on Instrumentation in Aerospace Simulation Facilitie. IEEE, pp. 168–178. https://doi.org/10.1109/ICIASF.1989.77670.

Gad-el Hak, M., Bushnell, D.M., 1991. Separation control: review. J. Fluids Eng. 113 (1), 5–30. https://doi.org/10.1115/1.2926497.

Lee, D.D., Seung, H.S., 1999. Learning the parts of objects by non-negative matrix factorization. Nature 401 (6755), 788–791. https://doi.org/10.1038/44565.

Medina, P., Schreck, S., Johansen, J., Fingersh, L., 2011. Oil-flow visualization on a SWT-2.3-101 wind turbine. 29th AIAA Applied Aerodynamics Conference. American Institute of Aeronautics and Astronautics (AIAA), pp. 2011–3818. https://doi.org/10.2514/6.2011-3818.

Montelpare, S., Ricci, R., 2004. A thermographic method to evaluate the local boundary layer separation phenomena on aerodynamic bodies operating at low Reynolds number. Int. J. Therm. Sci. 43 (3), 315–329. https://doi.org/10.1016/j.ijthermalsci.2003.07.006.

Quast, A., 1987. Detection of transition by infrared image techniques. 12th International Congress on Instrumentation in Aerospace Simulation Facilities.

Richter, K., Koch, S., Goerttler, A., Ltke, B., Wolf, C., Benkel, A., 2015. Unsteady boundary layer transition on the DSA-9a rotor blade airfoil. 41th European Rotorcraft Forum.

Schlichting, H., 1979. Boundary-Layer Theory. McGraw-Hill.

Swytink-Binnema, N., Johnson, D.A., 2016. Digital tuft analysis of stall on operational wind turbines. Wind Energy 19 (4), 703–715. https://doi.org/10.1002/we.1860.

Wolf, C.C., Mertens, C., Gardner, A.D., Dollinger, C., Fischer, A., 2019. Optimization of differential infrared thermography for unsteady boundary layer transition measurement. Exp. Fluid 60 (1), 19. https://doi.org/10.1007/s00348-018-2667-0.